

Identification of catalytic sites for oxygen reduction and oxygen evolution in N-doped graphene materials: Development of highly efficient metal-free bifunctional electrocatalyst

Hong Bin Yang,¹ Jianwei Miao,¹ Sung-Fu Hung,² Jiazang Chen,¹ Hua Bing Tao,¹ Xizu Wang,³ Liping Zhang,¹ Rong Chen,¹ Jiajian Gao,¹ Hao Ming Chen,² Liming Dai,^{4*} Bin Liu^{1*}

2016 © The Authors, some rights reserved; exclusive licensee American Association for the Advancement of Science. Distributed under a Creative Commons Attribution NonCommercial License 4.0 (CC BY-NC). 10.1126/sciadv.1501122

Oxygen reduction reaction (ORR) and oxygen evolution reaction (OER) are critical to renewable energy conversion and storage technologies. Heteroatom-doped carbon nanomaterials have been reported to be efficient metal-free electrocatalysts for ORR in fuel cells for energy conversion, as well as ORR and OER in metal-air batteries for energy storage. We reported that metal-free three-dimensional (3D) graphene nanoribbon networks (N-GRW) doped with nitrogen exhibited superb bifunctional electrocatalytic activities for both ORR and OER, with an excellent stability in alkaline electrolytes (for example, KOH). For the first time, it was experimentally demonstrated that the electron-donating quaternary N sites were responsible for ORR, whereas the electron-withdrawing pyridinic N moieties in N-GRW served as active sites for OER. The unique 3D nanoarchitecture provided a high density of the ORR and OER active sites and facilitated the electrolyte and electron transports. As a result, the as-prepared N-GRW holds great potential as a low-cost, highly efficient air cathode in rechargeable metal-air batteries. Rechargeable zinc-air batteries with the N-GRW air electrode in a two-electrode configuration exhibited an open-circuit voltage of 1.46 V, a specific capacity of 873 mAh g⁻¹, and a peak power density of 65 mW cm⁻², which could be continuously charged and discharged with an excellent cycling stability. Our work should open up new avenues for the development of various carbon-based metal-free bifunctional electrocatalysts of practical significance.

INTRODUCTION

Renewable electrochemical energy conversion and storage technologies are promising in addressing global energy and environmental challenges (1, 2). Oxygen reduction reaction (ORR) and oxygen evolution reaction (OER) are two key electrochemical processes that take place in a wide range of renewable electrochemical energy conversion and storage devices, including rechargeable metal-air batteries, regenerative fuel cells, and water splitting cells (3–12). However, the overall efficiency of these devices has been severely limited by the sluggish kinetics in the electrocatalytic reduction and evolution of molecular oxygen (13–15). Therefore, noble metals and transition metal (Ni, Co, Mn, and Fe) catalysts have been widely used for electrocatalysis of ORR and OER (16, 17). Unfortunately, the scarcity, high cost, and inferior durability of these metal-based catalysts have hampered the widespread and large-scale applications of these renewable energy technologies.

Along with the extensive research and development of the noble metal-based ORR and OER catalysts (18–22), carbon nanomaterials (10), such as heteroatom-doped carbon nanotubes (CNTs) and graphene, have been studied as metal-free electrocatalysts for energy conversion and storage. Impressive experimental and theoretical results have been achieved through the molecular and/or nanoarchitecture

engineering of carbon nanomaterials using various innovative strategies, including surface functionalization (23–25), geometric structuring (26–30), and heteroatom doping (17, 31–34). Among them, nitrogen-doped carbon nanomaterials were demonstrated as efficient ORR (35–39) and OER (40, 41) electrocatalysts, respectively. More recently, metal-free N-, P-codoped carbon-based nanomaterials have been studied as bifunctional catalysts for both ORR and OER (42), as were N mono-doped carbon nanomaterials with unique structures (43, 44) and unknown bifunctional catalytic mechanisms. Therefore, to achieve cost-effective, high-performance, metal-free ORR and OER bifunctional electrocatalysts, it is highly desirable to gain a mechanistic understanding of metal-free electrocatalysis (particularly, OER) to guide the development of new catalytic materials with sufficient active sites.

Here, we have developed a novel strategy to synthesize N-doped graphene nanoribbons with interconnected three-dimensional (3D) architecture (that is, N-GRW). The as-prepared N-GRW exhibited superior overall electrocatalytic activities for both ORR and OER with an excellent stability in alkaline media, comparable to the state-of-the-art noble metal electrocatalysts (for example, Pt/C and Ir/C). For the first time, it was experimentally found that the electron-withdrawing pyridinic N moieties in the N-GRW served as active sites for OER, whereas the electron-donating quaternary N sites were responsible for ORR. The unique 3D nanoarchitecture ensured a high density of active sites as well as excellent mass and charge transport for both ORR and OER. As a result, the as-prepared N-GRW was demonstrated to be a promising low-cost, highly efficient air cathode in rechargeable metal-air batteries. Therefore, our study on the newly developed N-GRW has provided new concepts/principles for designing

¹School of Chemical and Biomedical Engineering, Nanyang Technological University, 62 Nanyang Drive, Singapore 637459, Singapore. ²Department of Chemistry, National Taiwan University, No. 1, Sec. 4, Roosevelt Road, Taipei 10617, Taiwan. ³Institute of Materials Research and Engineering (IMRE), Agency for Science, Technology and Research (A*STAR) #08-03, 2 Fusionopolis Way, Innovis, Singapore 138634, Singapore. ⁴Department of Macromolecular Science and Engineering, Case Western Reserve University, 10900 Euclid Avenue, Cleveland, OH 44106, USA.

*Corresponding author. E-mail: liming.dai@case.edu (L.D.); liubin@ntu.edu.sg (B.L.)

bifunctional catalysts by catalytic active site and nanoarchitecture engineering, which could open up new avenues for the development of sustainable energy conversion and storage technologies based on earth-abundant, scalable, and metal-free electrocatalysts.

RESULTS

Synthesis and structure characterization of N-doped graphene catalysts

In a typical experiment, we synthesized the N-GRW by first grinding a mixture of melamine and L-cysteine with a mass ratio of 4:1 into a homogeneous precursor (Fig. 1A), followed by a two-step carbonization under argon atmosphere (fig. S2). The results from our systematic investigations on the effects of the carbonization temperature and the melamine-to-L-cysteine ratio on the structural evolution (figs. S3 to S5) are consistent with the following scenario for the N-GRW formation. Initially, melamine was polymerized to form carbon nitride, whereas the thiol groups on L-cysteine covalently bonded with the newly formed carbon nitride plane via the formation of $-C-S-C-$ bonds, probably through a radical mechanism, because the thiol groups on L-cysteine are highly reactive and susceptible to hydrogen extraction by free radicals. X-ray photoelectron spectroscopic (XPS) measurements, shown in fig. S6, provide evidences for the formation of C_3N_4 and sulfur-doped C_3N_4 , whereas Fig. 1A indicates steric hindrances for the formation of the lateral $C-N=C$ bonds to impede the extension of the 2D carbon nitride plane due to the insertion of L-cysteine moieties. Thus, L-cysteine acted not only as a carbon source but also as a “template” to generate pores within the resultant carbon nitride. The formation of porous sulfur-doped carbon nitride was confirmed by the porous morphology (fig. S7) and larger surface area (fig. S8) observed for the sulfur-doped carbon nitride, with respect to the C_3N_4 sample prepared by polymerization of melamine with and without L-cysteine, respectively. As indicated by thermogravimetric analyses (TGAs) (fig. S9), subsequent thermal treatment of the sulfur-doped carbon nitride sample caused a marked mass loss over 600° to 800°C , arising from py-

rolysis of the sulfur-doped carbon nitride, which was accompanied by a significant reduction in the nitrogen content from 48 to 20 atomic % (fig. S10) and an increase in the specific surface area (from 78 to $480\text{ m}^2\text{ g}^{-1}$; fig. S11). The thermal treatment could lead to the formation of 3D interconnected carbon networks (that is, N-GRW) through chemical bonding (for example, $-C-S-C-$) between pyrolyzed L-cysteine molecules on the same or different C_3N_4 planes, along with the concomitant losses of nitrogen/sulfur from the decomposed L-cysteine moieties. Because of the strong $-C-S-C-$ bonding, no oxidation occurred during the carbonization below 800°C (fig. S12). The resultant N-GRW had a uniformly distributed 3D interconnected porous structure (Fig. 1, B and C, and fig. S4) with a nitrogen content as high as 20 atomic % (carbonized at 800°C) and 6 atomic % (carbonized at 1000°C). A higher carbonization temperature resulted in an improved graphitization degree and a reduced dopant content. The thiol group in L-cysteine was found to play critical and irreplaceable roles in controlling the structure of the N-GRW. By replacing L-cysteine with amino acids bearing other functional groups [for example, methyl (L-alanine) and hydroxyl (L-serine) groups] during the material synthesis, we could not produce N-GRW, but could only form N-doped graphene sheets with or without the porous structure (N-HGS or N-GS) (fig. S13), indicating once again the important role of the $-C-S-C-$ bonding to the porous network formation.

Figure 2A reproduces a typical SEM image of the as-synthesized N-GRW, which shows the 3D interconnected network nanoarchitecture. Transmission electron microscopy (TEM) and atomic force microscopy (AFM) analyses (Fig. 2, B to D) further affirm the uniform 3D structure of nanoribbon networks. Crumpled and entangled wrinkle-like structures can be seen in Fig. 2B, a common feature typically observed in porous N-doped graphene (31). The width of the nanoribbons is less than 20 nm (typically 10 nm), whereas the thickness measured by AFM (Fig. 2D) is less than 2.5 nm, corresponding to about eight or less layers of graphene sheets.

The measured specific surface area of the N-GRW is $\sim 530\text{ m}^2\text{ g}^{-1}$, significantly larger than that of the N-HGS ($480\text{ m}^2\text{ g}^{-1}$) and the N-GS ($460\text{ m}^2\text{ g}^{-1}$) (fig. S14 and table S1). Most of the pores in the N-GRW

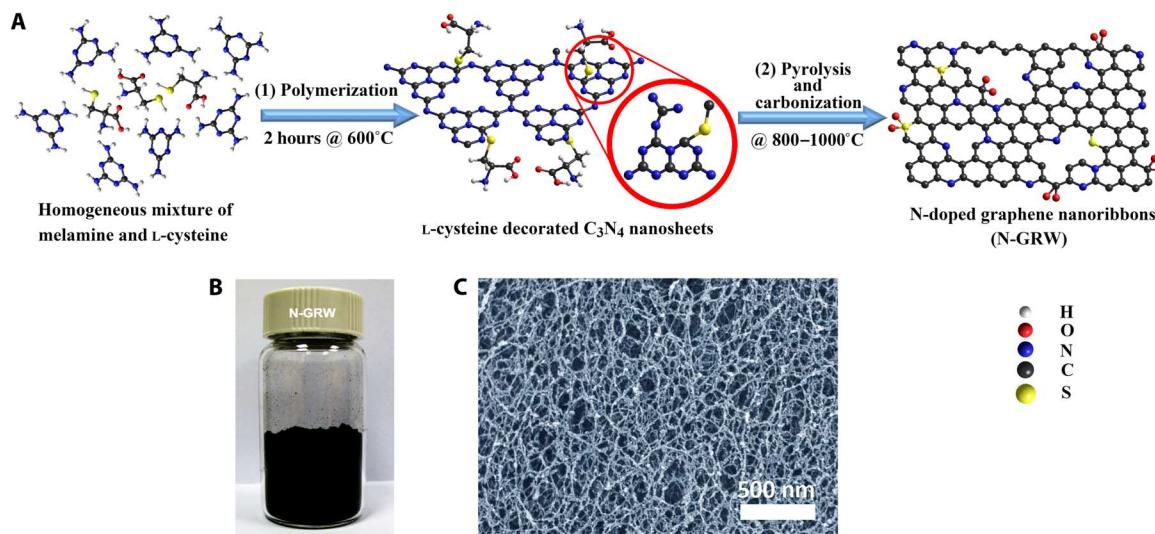


Fig. 1. Synthesis of N-GRW. (A) Synthesis steps: (1) polymerization at 600°C for 2 hours, and (2) pyrolysis and carbonization at 800° to 1000°C . (B) Digital photograph of the as-synthesized N-GRW. (C) Scanning electron microscopy (SEM) image of the as-synthesized N-GRW.

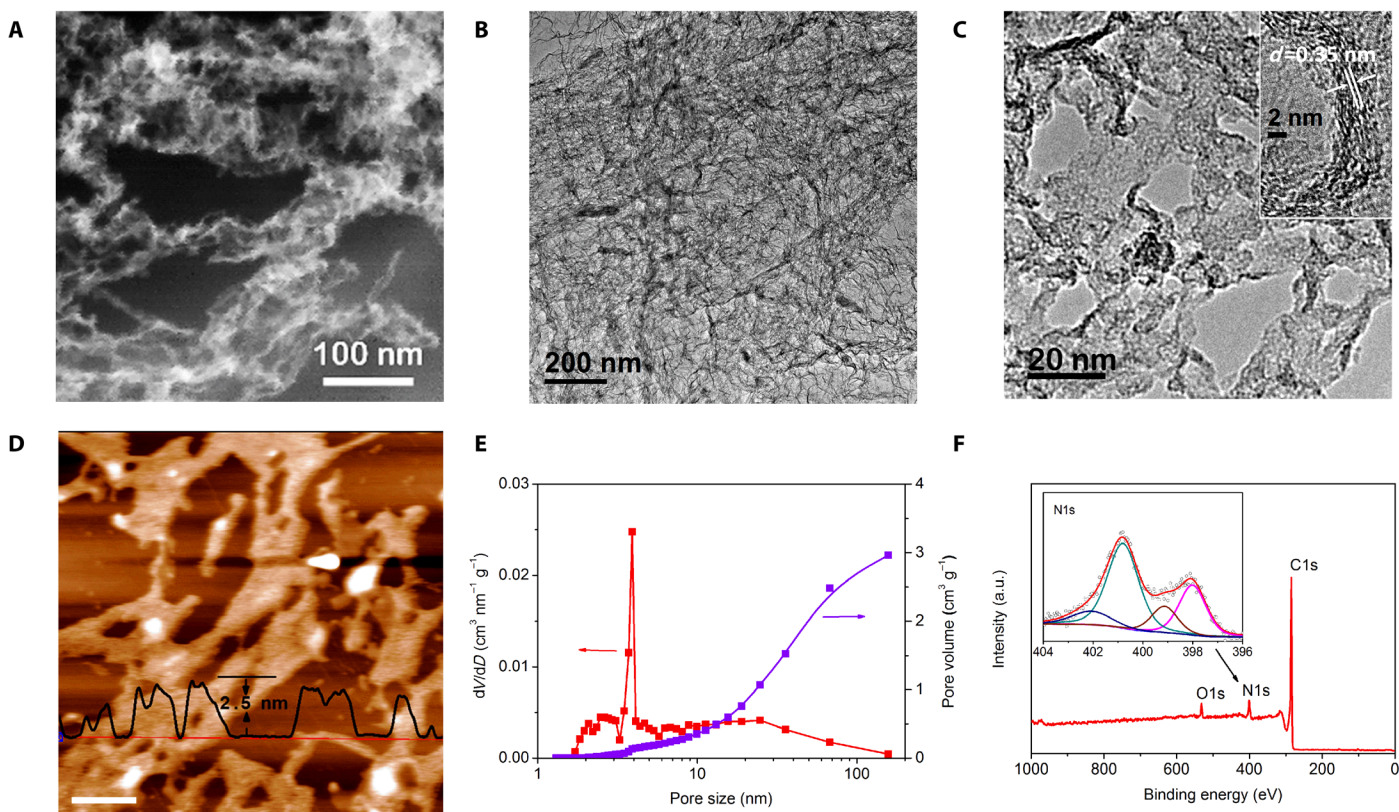


Fig. 2. Structure and composition of N-GRW. (A) High-resolution SEM image of the N-GRW. (B and C) Low-magnification (B) and high-magnification (C) TEM images of the N-GRW. (D) AFM image and height profile of the N-GRW on mica substrate (scale bar, 200 nm). (E) Barrett-Joyner-Halenda pore size distribution and pore volume of the N-GRW calculated from N_2 desorption isotherm. (F) XPS spectrum of the N-GRW. Inset shows a high-resolution N1s spectrum with peaks deconvoluted into pyridinic (397.8 eV), pyrrolic (398.9 eV), quaternary (400.8 eV), and oxidized (402.0 eV) N species. a.u., arbitrary units.

fall in the category of mesopores (Fig. 2E). The ultrahigh total pore volume of about $2.9 \text{ cm}^3 \text{ g}^{-1}$ for the N-GRW signifies the high porosity. The 3D porous N-GRW has abundant edges, thin walls, and conductive networks, which can facilitate fast transportation of mass and charge to facilitate electrochemical reactions.

Figure 2F displays the XPS survey spectrum for the N-GRW, whereas fig. S15 shows the high-resolution XPS C1s, N1s, and O1s spectra for the N-GRW, N-HGS, and N-GS. The corresponding numerical results are summarized in tables S1 and S2. It is clear from these XPS results that the N-GRW contains 5.9% N and 0.10% S. The content of S is much lower than that reported (around 2%) for other N-, S-codoped graphene materials (35, 36, 45, 46), possibly due to the different synthetic methods used and the relatively high carbonization temperature (1000°C) applied during our synthesis; this suggests that sulfur may just act as the bridge for the construction of the 3D nanoribbon networks, but without introducing any significant doping effect into the N-GRW (vide infra). The contents of N dopant in the N-HGS and N-GS are 5.4 and 6.1 atomic %, respectively, similar to that of the N-GRW. All samples show high contents of pyridinic N and quaternary N (1.45 and 2.8 atomic % for the N-GRW, 0.95 and 2.8 atomic % for the N-HGS, and 1.34 and 3.0 atomic % for the N-GS), which have been known to be active for ORR and other catalytic reactions (31, 47).

We further used x-ray diffraction (XRD) and Raman spectroscopy to investigate the crystalline structure and graphitization degree of the N-GRW, N-HGS, and N-GS samples. As shown in fig. S16, all samples

exhibit similar broad diffraction patterns characteristic of the carbon (002) over 25.8° , suggesting a low degree of crystallization. According to Scherrer's formula (48), the mean crystal size along the c -direction was calculated to be $\sim 1.8 \text{ nm}$. The relatively weak peak intensity for the N-GRW, with respect to the other two samples, indicates a defect-rich feature. On the other hand, Raman spectra for all of the N-doped graphene samples show two clear vibrational bands (the G band and D band). The I_D/I_G ratios were calculated to be 3.34, 2.34, and 2.10 for the N-GRW, N-HGS, and N-GS, respectively. A higher I_D/I_G ratio is usually associated with a more disordered carbon structure (46–48). I_D/I_G is inversely proportional to the in-plane coherence length (L_a), which is the mean average crystallite size of the sp^2 domains in the nano-graphite system and can be calculated from $L_a = C(\lambda)(I_D/I_G)^{-1}$, with $C(\lambda) = 43.5 \text{ \AA}$ for 514 nm (49, 50). The calculated L_a values are 1.3, 1.8, and 2.1 nm for the N-GRW, N-HGS, and N-GS, respectively, indicating that the average size of crystalline domains in the N-GRW is apparently smaller than that in the N-HGS and N-GS, which is consistent with the results obtained from the SEM and TEM images (figs. S3, S4, and S13). The smaller domain size observed for the N-GRW suggests that the N-GRW sample has more edge sites, as also confirmed by its lower sp^2/sp^3 ratio deduced from the high-resolution C1s spectra (0.36, 0.58, and 0.68 for the N-GRW, N-HGS, and N-GS, respectively; fig. S15). The graphene edge sites have recently been shown to have a much faster electron transfer rate and higher electrocatalytic activity than the graphene basal plane (51, 52). This, coupled with the fast

mass, as well as ionic and electronic transport, makes the N-GRW an ideal electrode for energy conversion and storage, as we should see later.

ORR and OER catalytic activity of N-doped graphene catalysts

To evaluate the electrocatalytic activities of the N-GRW, N-HGS, and N-GS toward ORR, we performed rotating ring-disc electrode (RRDE) measurements in alkaline electrolytes (figs. S17 and S18). Figure 3A reproduces the ORR polarization curves measured from the N-GRW, which shows an onset potential and a half-wave potential ($E_{1/2}$) of 0.92 and 0.84 V versus RHE (reversible hydrogen electrode), respectively. These values are very close to those of Pt/C (0.94 and 0.85 V), but much more positive than those of the N-HGS (0.90 and 0.81 V versus RHE) and N-GS (0.87 and 0.80 V versus RHE). The trend for the onset potential deduced from the RRDE measurements consists well with the CV scans (fig. S19). The ring current profiles associated with the reduction of peroxide species (HO_2^-) formed during the ORR process are shown in the upper half of Fig. 3A, from which the H_2O_2 yield on the N-GRW was calculated to be below 5%, a value that is comparable to that of the Pt/C catalyst but smaller than that of the N-HGS and N-GS catalysts. The electron transfer number per O_2 molecule was estimated to be ~ 3.95 for the N-GRW, which is obviously higher than that for the N-HGS and N-GS (fig. S20). The excellent ORR activity of the N-GRW catalyst was further confirmed by the

smaller Tafel slope of $53 \text{ mV decade}^{-1}$ at low overpotentials, as compared with that of Pt/C ($60 \text{ mV decade}^{-1}$) and N-GS ($69 \text{ mV decade}^{-1}$) in 1 M KOH (fig. S21). Furthermore, the N-GRW electrode also demonstrated a good methanol tolerance, much better resistance to CO poisoning (inset of Fig. 3B and figs. S22 and S23), and superior operational durability to Pt/C catalyst with only a 10% decay in ORR activity over a 12-hour continuous operation at a potential of 0.7 V versus RHE. Figure 3C and fig. S24 show the linear sweep voltammetry (LSV) and cyclic voltammetry (CV) scans, respectively, before and after accelerated degradation test (ADT). It was found that Pt/C experienced a marked loss (35%) in electrochemical active surface area (ECSA) after 2000 consecutive cycles (fig. S24). In contrast, almost no loss in ECSA was observed for the N-GRW under the same conditions, leading to a smaller half-wave potential negative shift (15 mV for the N-GRW versus 35 mV for Pt/C) and smaller limited current variation (fig. S24). These results indicate that the N-GRW is an efficient metal-free ORR catalyst with an electrocatalytic activity comparable to that of Pt/C, but with a superior methanol and CO tolerance, and operational stability. These results, together with the metal-free preparation procedure (Fig. 1), indicate that the observed electrocatalytic activity can be attributed exclusively to the incorporation of nitrogen in the 3D N-GRW (vide infra).

In addition to the superb ORR performance discussed above, we also tested OER activities for the N-GRW, N-HGS, and N-GS using RDE measurements in 1 M (Fig. 3D) and 0.1 M KOH (fig. S25). As can be

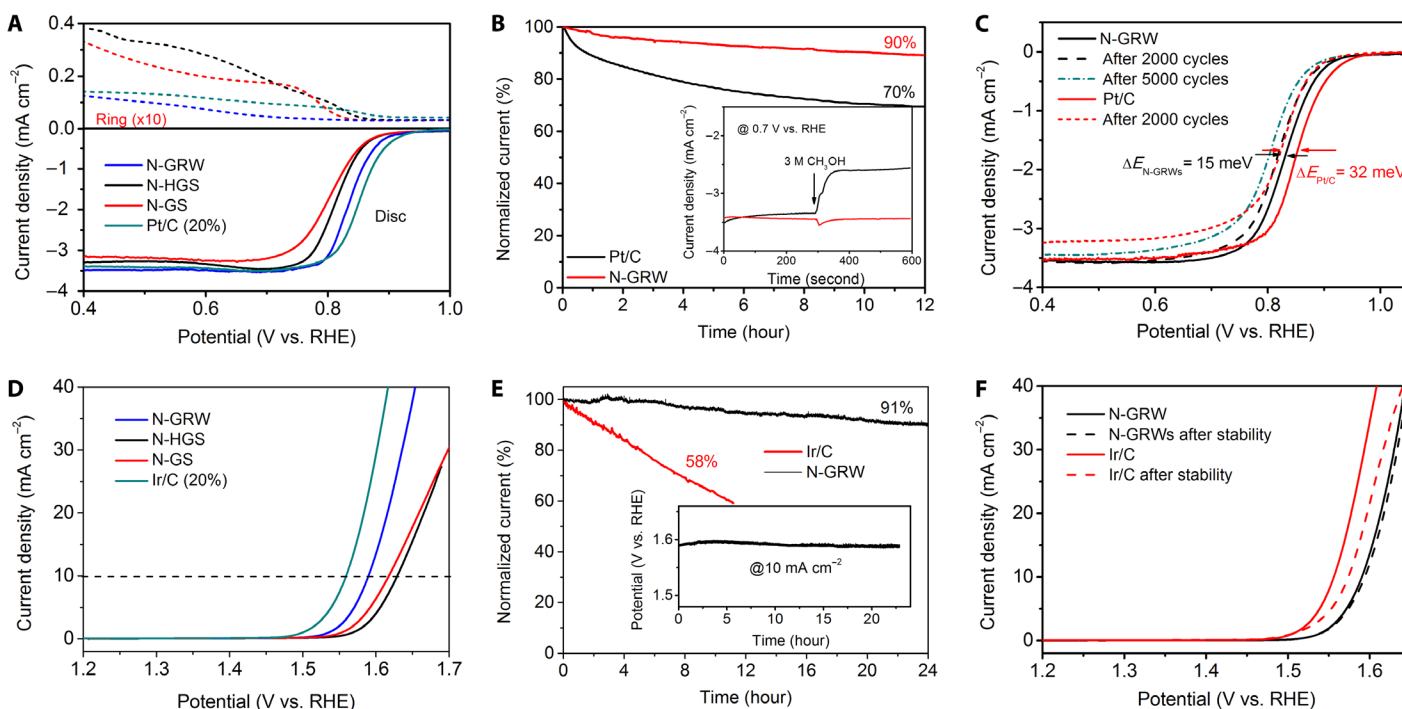


Fig. 3. Electrochemical performances of N-doped graphene catalysts for ORR and OER. (A) LSV curves of N-doped graphene catalysts on RRDE in O_2 -saturated 1 M KOH at a rotation speed of 1600 rpm and a scan rate of 5 mV s^{-1} , with a constant potential of 1.5 V versus RHE applied on the ring. Disc current is displayed on the lower half of the graph, whereas the ring current (dotted line) is shown on the upper half. (B) Chronoamperometric (current-time) responses of Pt/C and the N-GRW for ORR at 0.7 V versus RHE, in 1 M KOH, at a rotation speed of 900 rpm. Inset shows the crossover effect of the N-GRW and Pt/C electrodes at 0.7 V versus RHE, followed by introduction of methanol (3 M) in O_2 -saturated 1 M KOH. (C) LSV curves of the N-GRW before and after ADT, performed in 1 M KOH at a scan rate of 50 mV s^{-1} for the N-GRW and Pt/C. (D) LSV curves for OER on RDE for the N-GRW, N-HGS, and N-GS in O_2 -saturated 1 M KOH at a rotation speed of 1600 rpm and a scan rate of 5 mV s^{-1} . (E) Chronoamperometric (current-time) responses for OER at fixed overpotential of 320 mV (for Ir/C) and 360 mV (for the N-GRW). Inset shows chronopotentiometric (potential-time) response at a fixed current loading of 10 mA cm^{-2} . (F) LSV curves for OER before and after stability test for Ir/C and the N-GRW.

seen, the overpotential required to drive a 10 mA cm^{-2} current density (η_{10}) for the N-GRW is 360 mV, which is significantly lower than that for the N-HGS and N-GS (400 and 390 mV, respectively). Upon the application of potentials over the onset potential, the evolution of bubbles on the N-GRW electrode was evident. RRDE measurements (fig. S26) confirmed the production of oxygen bubbles with negligible HO_2^- formation, indicating a 4e pathway for OER on the N-GRW electrode in alkaline medium. The N-GRW exhibited the smallest Tafel slope of $47 \text{ mV decade}^{-1}$ within the OER region (fig. S27) in 1 M KOH among all the electrodes tested: N-HGS ($52 \text{ mV decade}^{-1}$), N-GS ($53 \text{ mV decade}^{-1}$), and Ir/C ($54 \text{ mV decade}^{-1}$). Therefore, our N-GRW catalyst is one of the best OER electrodes reported to date (table S3). CV curves of the N-GRW at different scan rates were recorded (fig. S28), showing that the contribution from double-layer capacitance of the electrode toward the measured current is negligible. Video S1 shows the gas evolution on the N-GRW-loaded carbon cloth electrode in a potential range from 1.5 to 1.8 V versus RHE, which also shows the firm attachment of catalysts on the carbon cloth electrode. Faradaic efficiency measurements carried out at 5 and 25 mA cm^{-2} revealed a nearly 100% Faradaic efficiency (fig. S29). Electrochemical stability of the N-GRW electrode was also tested, with the Ir/C as reference, under a fixed overpotential and current loading conditions over 24-hour continued electrolysis (Fig. 3E and inset). The N-GRW catalyst showed superior durability to Ir/C catalyst with $<10\%$ decay in the OER activity over 24 hours of continuous operation, which is consistent with the LSV results before and after the stability testing, as shown in Fig. 3F.

Identification of ORR and OER catalytic sites in N-doped graphene catalysts

To investigate mechanisms for the metal-free electrolysis of ORR and OER, we performed Mott-Schottky experiments to identify the doping states of the N-doped graphene catalysts. Depending on the N dopant configurations, N-doped graphene has been shown both theoretically and experimentally (53–56) to be either p-type or n-type. More specifically, n-type doping was found for quaternary/pyrrolic N and p-type doping for pyridinic N. Because the quaternary and pyridinic N are the dominating N components in our N-doped graphene catalysts (inset of Fig. 2D and fig. S15), both n-type and p-type domains should coexist in our samples. Mott-Schottky experiments were carried out in Ar-saturated 0.1 M KOH to identify doping states in the N-doped graphene catalysts. The results in the form of C_{scL}^{-2} versus E given in fig. S30 show both positive and negative slopes for the N-GRW, N-HGS, and N-GS in two different potential regions, confirming the presence of both n-type and p-type domains in our N-doped graphene samples with bipolar characteristics. The slopes of Mott-Schottky plots for the N-GRW, N-HGS, and N-GS in the n-type region (fig. S30A) are 4.2×10^7 , 5.1×10^7 , and $8.1 \times 10^7 \text{ C}^{-2}\cdot\text{V}$, respectively. This, together with the similar trend observed in the p-type region (fig. S30B), indicates that the N-GRW electrode has the highest charge carrier density (for both n-type and p-type carriers).

Recent DFT calculations have demonstrated that incorporated N itself could not act as active site for electrochemical reactions, but the adjacent C atoms have reduced energy barriers for ORR or OER due to the N-doping-induced charge redistribution in the π -conjugated system (57). Both experimental and theoretical studies (57–59) have indicated that quaternary N at the edge of graphene could act as the most active catalytic site for ORR by reducing the OOH intermediate adsorption energy. Figure 4A shows the similar ultraviolet photoelectron spectroscopy (UPS) spectra in valence band emission region for all samples tested.

In the high-resolution valence band region, the N-doping-induced features for the N-GRW (for example, N lone pair and $\pi_{\text{C-N}}$) could be seen (fig. S31). The work function (Φ) obtained from the UPS measurements is 4.42, 4.64, and 4.70 eV for the N-GRW, N-HGS, and N-GS, respectively. Thus, the N-GRW sample has a Fermi level (E_F) that is 0.22 eV higher than that of the N-HGS and 0.28 eV higher than that of the N-GS. Previous studies (60, 61) have shown that a catalyst with a smaller Φ could offer a lower energetic barrier (higher driving energy) for donating electrons from the surface of the catalyst to the adsorbed molecular oxygen, thereby facilitating the formation of the OOH species that is known to be the rate-determining step in the ORR process. Compared to the N-HGS and N-GS, the N-GRW sample has similar contents of the quaternary and pyrrolic N components for n-type doping, but much more edge sites associated with the constituent graphene nanoribbons in the 3D interconnected network. Therefore, having potentially more quaternary N edge sites and a relatively low energetic barrier for donating electrons from the surface of the catalyst to the adsorbed molecular oxygen, the N-GRW should be highly favorable for ORR with respect to the N-HGS and N-GS, as demonstrated by our experimental data (vide infra).

The correlation between the N-dopant state and OER activity is still largely lacking, though OER activities of N-doped carbon nanomaterials have been recently reported (41, 43). To elucidate the structure-performance relationship for facilitating the development of high-performance carbon-based OER catalysts, we performed x-ray absorption near-edge structure (XANES) spectroscopic measurements on carbon and nitrogen to identify the active sites for OER and ORR on the N-GRW electrode. Figure 4 (B and C) shows the evolution of carbon and nitrogen K-edge XANES spectra of the N-GRW catalyst before/after oxygen reduction and evolution reactions. On the basis of previous reports (62–66), the peaks of carbon and nitrogen in the K-edge XANES spectra were assigned, as indicated in Fig. 4 (B and C). The increase in peak intensity related to $\pi^*_{\text{C-O-C, C-N}}$ at 287.7 eV in Fig. 4B suggests adsorption of intermediate species (O^*) on carbon atoms in both ORR and OER processes, which is consistent with the appearance of a new peak at 289.6 eV (adsorption of OOH^* intermediates) after ORR and OER. The nitrogen K-edge XANES spectrum of the N-GRW after ORR, given in Fig. 4C, shows a new peak at the lower energy side of graphitic N (that is, quaternary N) ($\sim 401 \text{ eV}$), which can be ascribed to the distortion of heterocycles caused by the adsorbed O^* and OOH^* intermediates on carbon atoms near the graphitic N. In contrast, the peak at 398.0 eV related to pyridinic N was kept unchanged, with respect to the pristine N-GRW (Fig. 4C). These results indicate that the quaternary N with n-type doping, rather than the p-type doping by pyridinic N, is responsible for the ORR on the N-GRW electrode. However, after OER, the full width at half maximum of the pyridinic N peak at $\sim 398.0 \text{ eV}$ increased from 0.8 to 1.15 eV, together with the formation of a new peak at the higher energy side (Fig. 4C). In the meantime, other peaks, including the graphitic and pyrrolic N peaks, were kept nearly the same as those for the pristine N-GRW, indicating adsorption of OOH^* and O^* intermediates on carbon atoms next to the pyridinic N during OER, and hence, the pyridinic N with p-type doping is responsible for OER. As far as we are aware, this is the first experimental evidence for different N species in the N mono-doped carbon nanomaterials for metal-free catalysis of different reactions, which could lead to various bifunctional catalysts from other heteroatom mono-doped carbon nanomaterials.

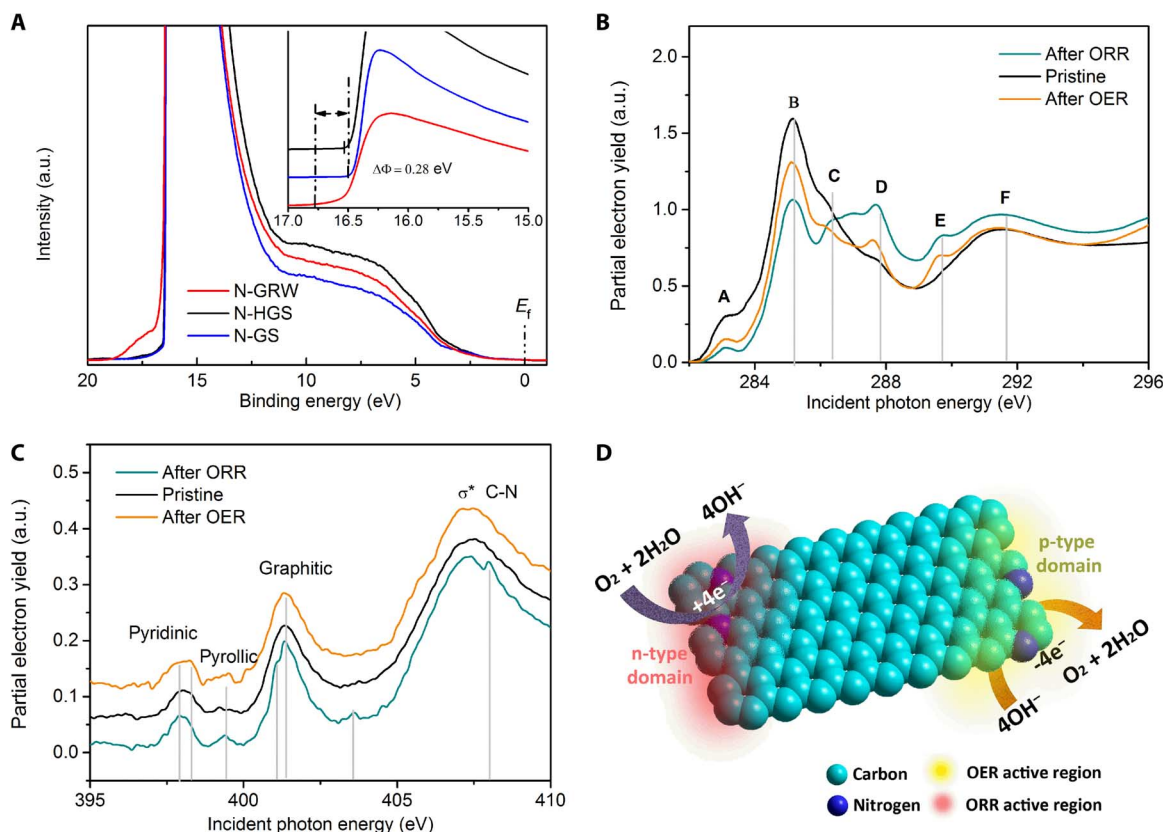


Fig. 4. Electronic characteristics and ORR/OER active sites of N-doped graphene catalysts. (A) UPS spectra collected using an He I (21.2 eV) radiation. Inset shows the enlarged view of the secondary electron tail threshold. (B and C) Carbon and nitrogen K-edge XANES spectra of N-GRW catalyst, acquired under ultrahigh vacuum, pristine (black line), after ORR (yellow line) and after OER (blue line). In carbon K-edge XANES spectra, A: defects, B: $\pi^*_{C=C}$, C: π^*_{C-OH} , D: π^*_{C-O-C} , E: $\pi^*_{C=O}$, F: σ^*_{C-C} . (D) Schematic diagram of ORR and OER occurring at different active sites on the n- and p-type domains of the N-GRW catalyst.

The observed influences of the graphitic N and pyridinic N on ORR and OER can also be understood from the doping-induced charge redistribution. As discussed above, the quaternary N atoms in graphene could provide electrons to the π -conjugated system (n-type doping), leading to an increased nucleophile strength for the adjacent carbon rings [$C(\delta^-)$] to enhance the O_2 adsorption [because O_2 has high densities of O lone pair electrons [$O(\delta^+)$]], and hence accelerating the ORR (67, 68). A similar scenario is applicable to the pyrrolic N atoms. As a result, carbon atoms near the quaternary N and/or pyrrolic N are not energetically favorable for adsorption of water oxidation intermediates (OH^- and OOH^-) in alkaline solution, and are thereby unfavorable for OER. However, pyridinic N (an electron-withdrawing group with the lone pair electrons involved in the resonance to delocalize electrons to make the N atoms electron-deficient) can accept electrons (p-type doping) from adjacent C atoms (δ^+), facilitating the adsorption of water oxidation intermediates (OH^- , OOH^-)—the rate-determining step for OER in alkaline solution (69, 70). Besides, the p-type domains of graphene can accept electrons from the adsorbed OH^- to the catalyst surface to further accelerate the intermediate step of $OH^- \rightarrow OH_{ads} + e^-$. A similar effect on OER has been revealed for the electron-withdrawing ketonic C=O group (40). Because the N-GRW sample contains higher amounts of the pyridinic N and ketonic (C=O) group (1.45 and 0.55 atomic %) than those of the N-HGS (0.95 and 0.28 atomic %) and N-GS (1.34 and 0.52 atomic %), the N-GRW ex-

hibited a higher OER activity than that of the N-HGS and N-GS. Therefore, the N-GRW can act as an efficient bifunctional electrocatalyst for both ORR and OER, though detailed effects of the doping-induced charge transfer on the catalytic mechanisms may be somewhat different under an applied potential in an electrochemical cell. On the basis of the above spectroscopic and electrochemical analyses, a schematic diagram was drawn in Fig. 4D as a working model for electrolysis of ORR and OER by the N-GRW. The turnover frequency (TOF) for the ORR and OER was calculated for the four-electron pathway, and the corresponding TOFs of N-GRW catalyst were 0.08 and 0.33 s^{-1} for ORR and OER, respectively. As shown in Fig. 4D, the separated active sites for ORR and OER at the n- and p-type domains of the N-GRW can prevent catalyst active sites from possible cross-deactivation during the ORR and OER processes and allow for an independent optimization of the catalytic performance on each of the two different type domains.

From the above discussions, we could conclude that the ORR activity decreased in the order of N-GRW > N-HGS > N-GS, whereas the OER activity decreased in the order of N-GRW > N-GS > N-HGS (Fig. 3, A and D, and fig. S32), matching with the amounts of active sites (quaternary N, pyrrolic N for ORR and pyridinic N, C=O for OER) in respective samples (table S2). To evaluate the overall ORR-OER bifunctional activities, we compared the overvoltage between OER and ORR ($\Delta E = E_{10} - E_{1/2}$), where E_{10} is the OER potential at a current density of 10 mA cm^{-2} and $E_{1/2}$ is the ORR half-wave potential for the

catalysts investigated in this study. Smaller ΔE corresponds to less efficiency loss and better catalyst performance as a reversible oxygen electrode. From Fig. 3 and figs. S18 and S25, we deduced a ΔE of 0.82 V in 0.1 M KOH and 0.75 V in 1 M KOH for the as-synthesized N-GRW, which is much lower than that of the N-HGS (0.92 and 0.82 V) and N-GS (0.92 and 0.82 V), reassuring the excellent bifunctional electrocatalytic activity for the N-GRW. As summarized in table S3, the bifunctional catalytic activity of the N-GRW is the best among recently reported high-performance bifunctional ORR/OER catalysts (6, 7, 38–44, 71, 72), including highly active metal-free carbon catalysts [for example, P-doped C_3N_4 , $\Delta E = 0.92$ V (7), N-MWCNT (multi-walled CNT), $\Delta E = 1.05$ V (43), N-graphene/CNT, $\Delta E = 0.93$ V

(44)] and even transition-metal oxide bifunctional catalysts [for example, $LiCoO_2$, $\Delta E = 0.97$ V (71) and $Mn_xO_y(Co_xO_y)/N$ -doped carbon, $\Delta E = 0.87$ V (72)]. Thus, the newly developed N-GRW electrode is of practical importance.

Rechargeable zinc-air batteries in two-electrode configuration

To demonstrate potential applications for the N-GRW sample in practical energy devices, we constructed a rechargeable zinc-air battery in two-electrode configuration using a hybrid electrode based on the N-GRW-loaded carbon cloth/gas diffusion layer as the air cathode (Fig. 5A and figs. S33 and S34). Before the test of the battery performance,

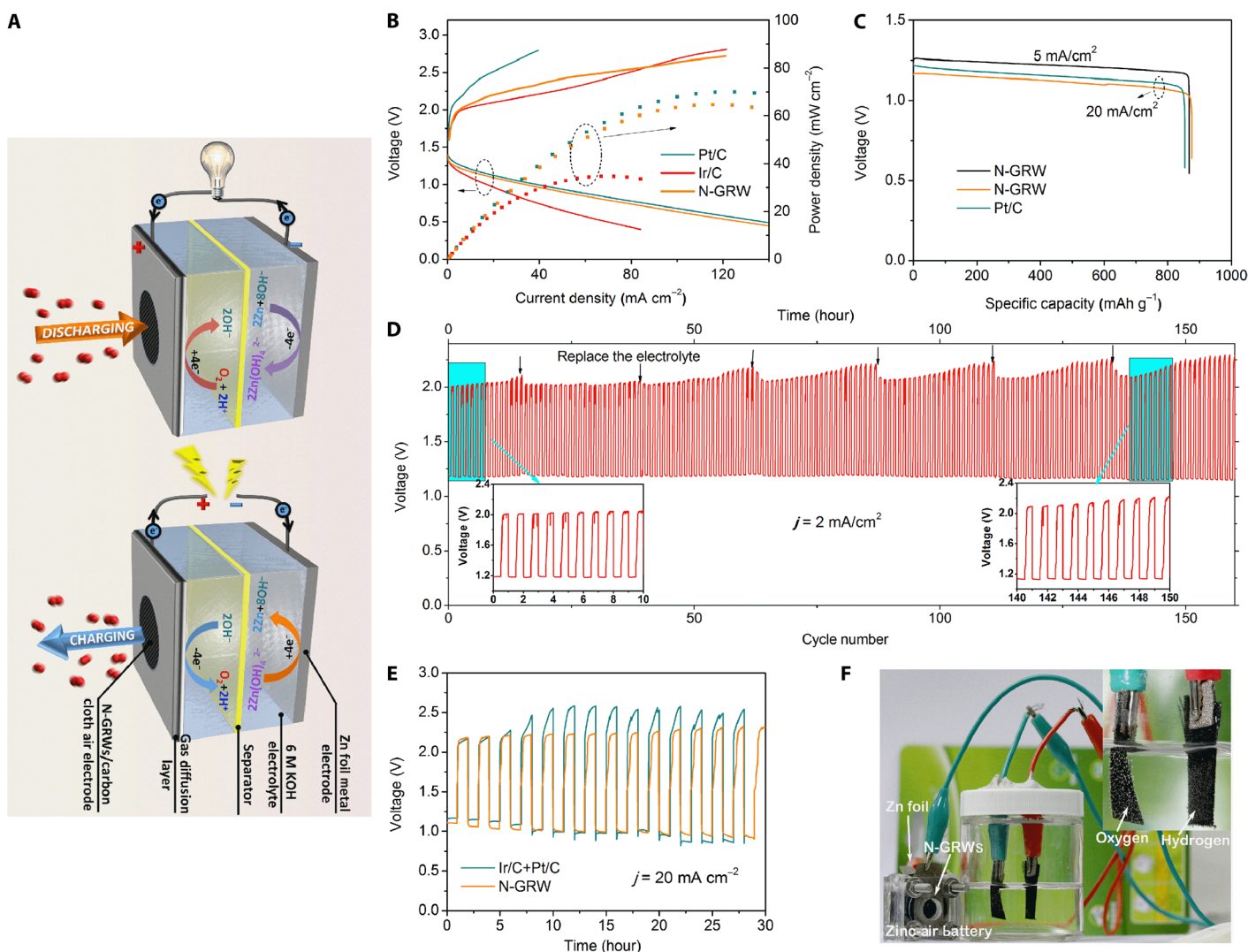


Fig. 5. Application of N-GRW bifunctional catalyst in rechargeable zinc-air batteries. (A) Schematic of a zinc-air battery at charging and discharging conditions. (B) Galvanodynamic charge/discharge profiles and power density curves of zinc-air batteries assembled from the N-GRW, Pt/C, Ir/C, and mixed Pt/C + Ir/C (1:1 by weight) air electrode (fig. S36), respectively. (C) Discharge curves of zinc-air batteries assembled from the N-GRW and Pt/C catalysts at 5 and 20 mA cm⁻² discharging rate. (D) Charging/discharge cycling at a current density of 2 mA cm⁻². Insets show the initial and after long-time cycling testing charging/discharging curves of a zinc-air battery assembled from N-GRW as air catalyst. (E) Charging/discharge cycling curves of zinc-air batteries assembled from the N-GRW (yellow line) and mixed Pt/C + Ir/C air electrode (blue line) at a current density of 20 mA cm⁻² (catalyst loading amount: 0.5 mg cm⁻² for mixed Pt/C + Ir/C). (F) Photograph of an electrolysis cell powered by a zinc-air battery. Inset shows the bubble formation on both cathode and anode electrodes. All zinc-air batteries were tested in air at room temperature (catalyst loading amount: 0.5 mg cm⁻² for all zinc-air batteries).

we evaluated the ORR and OER activities for the N-GRW air cathode in O₂-saturated 6 M KOH (fig. S35), along with the Pt/C, Ir/C, and carbon cloth as references. As can be seen in fig. S35B, the overall ORR-OER activity of the N-GRW air electrode is much better than that of the noble metal catalysts [for example, Pt/C (20%) and Ir/C (20%)]. Figure S35C shows that the N-GRW-loaded carbon cloth hybrid air cathode is very stable throughout the 20-hour continuous ORR/OER cycles at 5 mA cm⁻². Figure 5B reproduces polarization curves for the rechargeable zinc-air batteries in two-electrode configuration, which shows that the N-GRW electrode can supply a 20 mA cm⁻² discharge and charge current density at 1.09 and 2.18 V, outperformed the Pt/C (1.15 and 2.53) and Ir/C (0.95 and 2.05 V) air electrodes, and is comparable to the mixed Pt/C + Ir/C (1.06 and 2.07 V) (fig. S36) air electrode. The open-circuit voltage of the two-electrode zinc-air battery with the N-GRW air electrode is 1.46 V, which is the same as that for its counterpart with the Pt/C air electrode, but higher than that of the Ir/C (1.35 V) air electrode (fig. S37). The peak power density of the zinc-air battery assembled from the N-GRW air electrode is 65 mW cm⁻², with a specific capacity as high as 873 mAh g⁻¹ after being normalized to the mass of Zn (Fig. 5B). The drop of voltage in discharging as shown in Fig. 5C is due to reduction in electrolyte conductivity by forming carbonate between the electrolyte (KOH) and CO₂ in the atmosphere (73). Replacing air with pure oxygen can keep the cell voltage unchanged during discharging. The rechargeability of the secondary zinc-air battery using the N-GRW air electrode was tested by galvanostatic charging and discharging at 2 mA cm⁻² (Fig. 5D), showing a good cycling stability. However, as can be seen in Fig. 5, CO₂ in the atmosphere can affect the long-term stability during battery operation, and the influence of CO₂ is more severe on charging (OER) than discharging (ORR). Nevertheless, simple replenishment of the electrolyte and removal of CO₂ in air could regenerate and maintain the stable battery performance (fig. S38). Throughout more than 150 cycles of charging and discharging, the charge-discharge voltage gap of the two-electrode zinc-air battery with the N-GRW air electrode increased by only about 200 mV (Fig. 5D), verifying the excellent stability of the bifunctional N-GRW catalyst. Furthermore, the zinc-air battery assembled from the N-GRW air electrode could be rapidly charged and discharged at current densities as high as 20 mA cm⁻² with an outstanding stability, outperforming those devices assembled from the Pt/C, Ir/C, and mixed Pt/C + Ir/C air electrodes (Fig. 5E and fig. S39). After charging, the cell was disassembled and metallic zinc was observed deposited on the metal electrode, confirming the rechargeable feature of the zinc-air battery assembled from N-GRW air electrode (fig. S40). As an example for practical applications, a single zinc-air battery assembled from the N-GRW air electrode was used to power an electrolysis cell to split water into hydrogen and oxygen, as shown in Fig. 5F and video S2. Upon connecting the electrolysis cell to the zinc-air battery, the evolution of H₂ and O₂ was observed on the Pt/carbon cloth cathode and NiFe layer double hydroxide anode, respectively (videos S2 and S3).

DISCUSSION

We have developed a low-cost and scalable method to prepare novel 3D interconnected N-doped graphene nanoribbon network (N-GRW) architectures. The resultant N-GRW has a high density of electron-donating quaternary N favorable for ORR and high contents of

electron-withdrawing functional groups (pyridinic N, C=O) attractive for OER. Moreover, the high content of nitrogen doping could modify the charge distribution in the carbon ring, leading to increased C1s binding energy and inhibition of carbon corrosion during the OER. This, together with the 3D interconnected network architecture of a high specific surface area, large pore volume, and suitable pore size distribution, provides a synergistic effect to create superb catalytic activities and stability for both ORR and OER, outperforming the reported metal-free carbon catalysts and even transition-metal oxide bifunctional catalysts. Two-electrode zinc-air batteries, based on the bifunctional N-GRW air electrode with region-specific active sites for ORR and OER, could be stably charged and discharged over 150 cycles at 2 mA cm⁻². During discharging, the batteries exhibited an open-circuit voltage of 1.46 V, a specific capacity of 873 mAh g⁻¹, and a peak power density of 65 mW cm⁻². Furthermore, the rechargeable zinc-air batteries could be rapidly charged and discharged at charging and discharging current densities as high as 20 mA cm⁻² over 30 hours with an excellent cycling stability. Our work demonstrated the multiple independent electrocatalysis of different reactions by introducing multiple dopant states through single heteroatom doping carbon nanostructures, and for the first time, we detected different metal-free catalytic sites associated with different N species in the N mono-doped carbon nanomaterials. This, together with the unprecedented ORR-OER bifunctional electrocatalytic activity and battery performance observed for our newly developed N-GRW metal-free catalysts, should have important implications for the development of low-cost, scalable synthetic methodology for producing various new carbon-based metal-free catalysts for a large variety of electrochemical and catalytic applications.

MATERIALS AND METHODS

Materials

All chemicals—melamine (99%), L-cysteine (98%), L-serine (99%), L-alanine (99%), potassium hydroxide (99%), zinc chloride (≥98%), and zinc foil (thickness: 0.20 mm, purity: 99.9%)—were purchased from Sigma-Aldrich and used without further purification. Commercial noble metal catalysts Ir/C (20% Ir on Vulcan XC-72) and Pt/C (20% Pt on Vulcan XC-72) were purchased from Premetek.

Materials synthesis

In a typical synthesis of nitrogen-doped graphene nanoribbons (N-GRW) with interconnected 3D network architecture, a mixture of melamine and L-cysteine with a mass ratio of 4:1 was first ground into a homogeneous precursor in a ZrO₂ mortar. Subsequently, the fine powder mixture underwent a pyrolysis and carbonization process in a tubular furnace (Carbolite) under argon atmosphere. Detailed temperature and time profiles for the pyrolysis and carbonization processes are shown in fig. S2. For the synthesis of holey nitrogen-doped graphene sheets (N-HGS) and nitrogen-doped graphene sheets (N-GS), the L-cysteine precursor was replaced by L-alanine and L-serine while keeping the same molar ratio to melamine as in the synthesis of the N-GRW.

Electrochemical measurements

To prepare catalyst ink for the ORR and OER testing, 5 mg of catalyst and 25 μl of 5% Nafion 117 solution (DuPont) were introduced into

975 μl of 1:1 water/isopropanol solution sonicated for 3 hours. All potentials were calibrated with respect to RHE scale according to the Nernst equation ($E_{\text{RHE}} = E_{\text{Ag/AgCl}} + 0.059 \times \text{pH} + 0.197 \text{ V}$). Mott-Schottky analysis was carried out at a dc potential range of 0 to 1.2 V versus RHE (scan from 1.2 to 0 V, anodic scan) and 1.0 to 2.0 V versus RHE (scan from 1.0 to 2.0 V, cathodic scan). For the ORR test, an aliquot of 24 μl of the catalyst ink was applied onto a glassy carbon RDE or RRDE, giving a catalyst loading of 0.6 mg cm^{-2} . For the OER test, a catalyst loading of 0.3 mg cm^{-2} was applied onto the test electrode. RRDE measurements were conducted at 25°C in an oxygen-saturated KOH solution at a scan rate of 5 mV s^{-1} and a rotation speed of 1600 rpm. Commercial 20 wt % Pt and 20 wt % Ir on Vulcan carbon black (Pt/C and Ir/C from Premetek) were measured for comparison.

X-ray absorption near-edge structure

The K-edge x-ray absorption spectra of C and N were measured in total electron yield mode at room temperature using BL-20A at the National Synchrotron Radiation Research Center (Hsinchu, Taiwan). Before XANES measurements, the samples were reacted in an O_2 -saturated 1 M KOH for 1 hour at 0.55 and 1.65 V versus RHE for ORR and OER, respectively. After ORR and OER, samples were soaked dry in vacuum and then subjected to an ultrahigh vacuum chamber (1×10^{-9} torr) for the total electron yield x-ray absorption spectra (TEY-XAS) collection. For C and N K-edge absorption, the data were collected at the 6-m high-energy spherical grating monochromator beamline with $10 \times 10\text{-}\mu\text{m}$ opening slits, corresponding to $\sim 0.08\text{-eV}$ energy resolution.

Rechargeable zinc-air battery

Rechargeable zinc-air battery in two-electrode configuration was assembled according to the following procedure: first, the air electrode was made by dipping a pretreated carbon cloth substrate ($1 \times 2 \text{ cm}^2$) into a bottle filled with 5 ml of catalyst ink (2 mg ml^{-1}), gently shaking for 1 hour, followed by drying in air. This process was repeated once to reach a catalyst loading of about 0.5 mg cm^{-2} . Subsequently, the catalyst-loaded carbon cloth was attached to a gas diffusion layer (AvCarb P75T, Fuel Cell Store) to form a carbon cloth/gas diffusion layer hybrid electrode for rechargeable zinc-air battery assembly. The electrolyte used was 6 M KOH filled with 0.2 M ZnCl_2 to ensure reversible zinc electrochemical reactions at the anode.

SUPPLEMENTARY MATERIALS

Supplementary material for this article is available at <http://advances.sciencemag.org/cgi/content/full/2/4/e1501122/DC1>

Experimental Section

- fig. S1. Molecular structures of precursors.
 fig. S2. Temperature and time profile of pyrolysis and carbonization process.
 fig. S3. FESEM images of the sample after pyrolysis at different temperatures.
 fig. S4. Low-magnification FESEM image of the N-GRW.
 fig. S5. FESEM images of samples prepared with different melamine-to-L-cysteine ratios.
 fig. S6. XPS spectra of C_3N_4 and S-doped C_3N_4 .
 fig. S7. TEM and FESEM images of C_3N_4 and S-doped C_3N_4 .
 fig. S8. Nitrogen adsorption isotherms of C_3N_4 and S-doped C_3N_4 .
 fig. S9. TGA and heat flow curves of S-doped C_3N_4 .
 fig. S10. XPS spectra of S-doped C_3N_4 and S-doped C_3N_4 carbonized at 800°C.
 fig. S11. Nitrogen adsorption isotherms of S-doped C_3N_4 and S-doped C_3N_4 carbonized at 800°C.
 fig. S12. S2p core XPS spectra of S-doped C_3N_4 and S-doped C_3N_4 carbonized at 800° to 1000°C.
 fig. S13. FESEM and TEM images of N-HGS and N-GS.
 fig. S14. Nitrogen adsorption isotherms and pore size distribution of N-doped graphene samples.
 fig. S15. C1s, N1s, and O1s core level high-resolution XPS spectra of the N-GRW, N-HGS, and N-GS.

- fig. S16. XRD patterns and Raman spectra of the N-GRW, N-HGS, and N-GS.
 fig. S17. LSV of N-doped graphene samples at different rotation speeds in the ORR region.
 fig. S18. Linear sweeping voltammograms and Koutecky-Levich plots of different catalysts in the ORR region.
 fig. S19. Cyclic voltammograms of N-doped graphene catalysts and Pt/C (20%) in Ar- and O_2 -saturated 1 M KOH.
 fig. S20. Peroxide yield and electron transfer number of N-doped graphene catalysts.
 fig. S21. Tafel plots of N-doped graphene catalysts in ORR region.
 fig. S22. Cyclic voltammograms of Pt/C and the N-GRW electrode in O_2 -saturated 0.1 M KOH filled with methanol.
 fig. S23. Current-time response of Pt/C and N-GRW for ORR with/without introducing CO into the electrolyte.
 fig. S24. Cycling durability of Pt/C and N-GRW.
 fig. S25. Linear sweeping voltammograms and Tafel plots of N-doped graphene catalysts in the OER region.
 fig. S26. RRDE measurements for the detection of H_2O_2 and O_2 generated during the OER process.
 fig. S27. OER Tafel plots of N-doped graphene catalysts.
 fig. S28. Cyclic voltammograms of the N-GRW in the OER region at different scan rates.
 fig. S29. Faraday efficiency of OER measurement.
 fig. S30. Mott-Schottky plots of N-doped graphene catalysts in two potential regions.
 fig. S31. XPS valence band spectra of the N-GRW.
 fig. S32. Nyquist plots of N-doped graphene samples in the ORR and OER regions.
 fig. S33. The assembly processes for preparation of hybrid air cathode.
 fig. S34. The assembly processes for the fabrication of a rechargeable zinc-air battery.
 fig. S35. ORR and OER performances of air cathode tested in half-cell configuration.
 fig. S36. Charge/discharge profiles and power density curves of zinc-air batteries assembled from mixed Pt/C + Ir/C air electrode.
 fig. S37. Open-circuit voltage profiles of zinc-air batteries.
 fig. S38. Charging/discharging cycling curves of the N-GRW-loaded electrode at charging/discharging current densities of 2 mA cm^{-2} .
 fig. S39. Charging/discharging cycling curves of Pt/C and Ir/C electrodes at charging/discharging current densities of 20 mA cm^{-2} .
 fig. S40. XRD patterns of materials detached from Ti foil after long time charging.
 note S1. XPS study of C3N4 and S-doped C3N4 samples.
 note S2. Deconvolution of C1s, N1s, and O1s XPS spectra of N-doped graphene samples.
 note S3. Average crystallite size of the sp^2 domains of N-doped graphene samples from Raman spectra.
 note S4. Brief explanation of ac impedance of N-doped graphene samples.
 table S1. Structural and compositional parameters of nitrogen-doped graphene catalysts.
 table S2. Surface nitrogen and oxygen species concentrations of nitrogen-doped graphene catalysts.
 table S3. Comparison of ORR and OER performances of our N-doped graphene nanoribbon networks with the recently reported highly active bifunctional catalysts.
 video S1. The evolution of O_2 bubbles at potentials from 1.6 to 1.8 V versus RHE.
 videos S2 and S3. The demonstration of water splitting driven by a single zinc-air battery.

REFERENCES AND NOTES

1. R. Schlögl, The role of chemistry in the energy challenge. *ChemSusChem* **3**, 209–222 (2010).
2. G. Centi, S. Perathoner, Towards solar fuels from water and CO_2 . *ChemSusChem* **3**, 195–208 (2010).
3. I. Katsounaros, S. Cherevko, A. R. Zeradjanin, K. J. Mayrhofer, Oxygen electrochemistry as a cornerstone for sustainable energy conversion. *Angew. Chem. Int. Ed.* **53**, 102–121 (2014).
4. A. Fujishima, K. Honda, Electrochemical Photolysis of water at a semiconductor electrode. *Nature* **238**, 37–38 (1972).
5. Y. Liang, Y. Li, H. Wang, J. Zhou, J. Wang, T. Regier, H. Dai, Co_3O_4 nanocrystals on graphene as a synergistic catalyst for oxygen reduction reaction. *Nat. Mater.* **10**, 780–786 (2011).
6. W. T. Hong, M. Risch, K. A. Stoerzinger, A. Grimaud, J. Suntivich, Y. Shao-Horn, Toward the rational design of non-precious transition metal oxides for oxygen electrocatalysis. *Energy Environ. Sci.* **8**, 1404–1427 (2015).
7. T. Y. Ma, J. Ran, S. Dai, M. Jaroniec, S. Z. Qiao, Phosphorus-doped graphitic carbon nitrides grown in situ on carbon-fiber paper: Flexible and reversible oxygen electrodes. *Angew. Chem. Int. Ed.* **54**, 4646–4650 (2015).
8. Y.-C. Lu, Z. Xu, H. A. Gasteiger, S. Chen, K. Hamad-Schifferli, Y. Shao-Horn, Platinum-gold nanoparticles: A highly active bifunctional electrocatalyst for rechargeable lithium-air batteries. *J. Am. Chem. Soc.* **132**, 12170–12171 (2010).
9. G. Wu, N. H. Mack, W. Gao, S. Ma, R. Zhong, J. Han, J. K. Baldwin, P. Zelenay, Nitrogen-doped graphene-rich catalysts derived from heteroatom polymers for oxygen reduction in nonaqueous lithium- O_2 battery cathodes. *ACS Nano* **6**, 9764–9776 (2012).

10. Q. Li, R. Cao, J. Cho, G. Wu, Nanocarbon electrocatalysts for oxygen reduction in alkaline media for advanced energy conversion and storage. *Adv. Eng. Mater.* **4**, 1301415–1301433 (2014).
11. S. Chen, J. Duan, M. Jaroniec, S. Z. Qiao, Three-dimensional N-doped graphene hydrogel/NiCo double hydroxide electrocatalysts for highly efficient oxygen evolution. *Angew. Chem. Int. Ed.* **52**, 13567–13570 (2013).
12. S. Chen, J. Duan, J. Ran, M. Jaroniec, S. Z. Qiao, N-doped graphene film-confined nickel nanoparticles as a highly efficient three-dimensional oxygen evolution electrocatalyst. *Energy Environ. Sci.* **6**, 3693–3699 (2013).
13. M. K. Debe, Electrocatalyst approaches and challenges for automotive fuel cells. *Nature* **486**, 43–51 (2012).
14. M. Piana, S. Catanorchi, H. A. Gasteiger, Kinetics of non-platinum group metal catalysts for the oxygen reduction reaction in alkaline medium. *ECS Trans.* **16**, 2045–2055 (2008).
15. T. R. Cook, D. K. Dogutan, S. Y. Reece, Y. Surendranath, T. S. Teets, D. G. Nocera, Solar energy supply and storage for the legacy and nonlegacy worlds. *Chem. Rev.* **110**, 6474–6502 (2010).
16. Y. Jiao, Y. Zheng, M. Jaroniec, S. Z. Qiao, Design of electrocatalysts for oxygen- and hydrogen-involving energy conversion reactions. *Chem. Soc. Rev.* **44**, 2060–2086 (2015).
17. J. Duan, S. Chen, M. Jaroniec, S. Z. Qiao, Heteroatom-doped graphene-based materials for energy-relevant electrocatalytic processes. *ACS Catal.* **5**, 5207–5234 (2015).
18. V. R. Stamenkovic, B. Fowler, B. S. Mun, G. Wang, P. N. Ross, C. A. Lucas, N. M. Marković, Improved oxygen reduction activity on Pt₃Ni(111) via increased surface site availability. *Science* **315**, 493–497 (2007).
19. C. Chen, Y. Kang, Z. Huo, Z. Zhu, W. Huang, H. L. Xin, J. D. Snyder, D. Li, J. A. Herron, M. Mavrikakis, M. Chi, K. L. More, Y. Li, N. M. Markovic, G. A. Somorjai, P. Yang, V. R. Stamenkovic, Highly crystalline multimetallic nanoframes with three-dimensional electrocatalytic surfaces. *Science* **343**, 1339–1343 (2014).
20. Y. Lee, J. Suntivich, K. J. May, E. E. Perry, Y. Shao-Horn, Synthesis and activities of rutile IrO₂ and RuO₂ nanoparticles for oxygen evolution in acid and alkaline solutions. *J. Phys. Chem. Lett.* **3**, 399–404 (2012).
21. T. Nakagawa, C. A. Beasley, R. W. Murray, Efficient electro-oxidation of water near its reversible potential by a mesoporous IrO_x nanoparticle film. *J. Phys. Chem. C* **113**, 12958–12961 (2009).
22. G. Wu, K. L. More, C. M. Johnston, P. Zelenay, High-performance electrocatalysts for oxygen reduction derived from polyaniline, iron, and cobalt. *Science* **332**, 443–447 (2011).
23. M. Steenackers, A. M. Gigler, N. Zhang, F. Deubel, M. Seifert, L. H. Hess, C. H. Y. X. Lim, K. P. Loh, J. A. Garrido, R. Jordan, M. Stutzmann, I. D. Sharp, Polymer brushes on graphene. *J. Am. Chem. Soc.* **133**, 10490–10498 (2011).
24. S. M. Kang, S. Park, D. Kim, S. Y. Park, R. S. Ruoff, H. Lee, Simultaneous reduction and surface functionalization of graphene oxide by mussel-inspired chemistry. *Adv. Funct. Mater.* **21**, 108–112 (2011).
25. T. Y. Ma, S. Dai, M. Jaroniec, S. Z. Qiao, Graphitic carbon nitride nanosheet-carbon nanotube three-dimensional porous composites as high-performance oxygen evolution electrocatalysts. *Angew. Chem. Int. Ed.* **53**, 7281–7285 (2014).
26. L. Jiao, X. Wang, G. Diankov, H. Wang, H. Dai, Facile synthesis of high-quality graphene nanoribbons. *Nat. Nanotechnol.* **5**, 321–325 (2010).
27. D. Yu, K. Goh, H. Wang, L. Wei, W. Jiang, Q. Zhang, L. Dai, Y. Chen, Scalable synthesis of hierarchically structured carbon nanotube-graphene fibres for capacitive energy storage. *Nat. Nanotechnol.* **9**, 555–562 (2014).
28. L. Ci, L. Song, D. Jariwala, A. L. Elias, W. Gao, M. Terrones, P. M. Ajayan, Graphene shape control by multistage cutting and transfer. *Adv. Mater.* **21**, 4487–4491 (2009).
29. L. Jiao, L. Zhang, X. Wang, G. Diankov, H. Dai, Narrow graphene nanoribbons from carbon nanotubes. *Nature* **458**, 877–880 (2009).
30. Y.-Z. Tan, B. Yang, K. Parvez, A. Narita, S. Osella, D. Beljonne, X. Feng, K. Müllen, Atomically precise edge chlorination of nanographenes and its application in graphene nanoribbons. *Nat. Commun.* **4**, 2646–2652 (2013).
31. X.-H. Li, M. Antonietti, Polycondensation of boron- and nitrogen-codoped holey graphene monoliths from molecules: Carbo-catalysts for selective oxidation. *Angew. Chem. Int. Ed.* **52**, 4572–4576 (2013).
32. J. P. Paraknowitsch, A. Thomas, Doping carbons beyond nitrogen: An overview of advanced heteroatom doped carbons with boron, sulphur and phosphorus for energy applications. *Energy Environ. Sci.* **6**, 2839–2855 (2013).
33. X. Wang, X. Li, L. Zhang, Y. Yoon, P. K. Weber, H. Wang, J. Guo, H. Dai, N-doping of graphene through electrothermal reactions with ammonia. *Science* **324**, 768–771 (2009).
34. X. Wang, G. Sun, P. Routh, D.-H. Kim, W. Huang, P. Chen, Heteroatom-doped graphene materials: Syntheses, properties and applications. *Chem. Soc. Rev.* **43**, 7067–7098 (2014).
35. J. Liang, Y. Jiao, M. Jaroniec, S. Z. Qiao, Sulfur and nitrogen dual-doped mesoporous graphene electrocatalyst for oxygen reduction with synergistically enhanced performance. *Angew. Chem. Int. Ed.* **51**, 11496–11500 (2012).
36. Z. Ma, S. Dou, A. Shen, L. Tao, L. Dai, S. Wang, Sulfur-doped graphene derived from cycled lithium-sulfur batteries as a metal-free electrocatalyst for the oxygen reduction reaction. *Angew. Chem. Int. Ed.* **54**, 1888–1892 (2015).
37. J. Shui, M. Wang, F. Du, L. Dai, N-doped carbon nanomaterials are durable catalysts for oxygen reduction reaction in acidic fuel cells. *Sci. Adv.* **1**, e1400129 (2015).
38. S. Chen, J. Duan, M. Jaroniec, S. Z. Qiao, Nitrogen and oxygen dual-doped carbon hydrogel film as a substrate-free electrode for highly efficient oxygen evolution reaction. *Adv. Mater.* **26**, 2925–2930 (2014).
39. Y. Li, W. Zhou, H. Wang, L. Xie, Y. Liang, F. Wei, J.-C. Idrobo, S. J. Pennycook, H. Dai, An oxygen reduction electrocatalyst based on carbon nanotube-graphene complexes. *Nat. Nanotechnol.* **7**, 394–400 (2012).
40. X. Lu, W.-L. Yim, B. H. R. Suryanto, C. Zhao, Electrocatalytic oxygen evolution at surface-oxidized multiwall carbon nanotubes. *J. Am. Chem. Soc.* **137**, 2901–2907 (2015).
41. Y. Zhao, R. Nakamura, K. Kamiya, S. Nakanishi, K. Hashimoto, Nitrogen-doped carbon nanomaterials as non-metal electrocatalysts for water oxidation. *Nat. Commun.* **4**, 2390 (2013).
42. J. Zhang, Z. Zhao, Z. Xia, L. Dai, A metal-free bifunctional electrocatalyst for oxygen reduction and oxygen evolution reactions. *Nat. Nanotechnol.* **10**, 444–452 (2015).
43. G.-L. Tian, Q. Zhang, B. Zhang, Y.-G. Jin, J.-Q. Huang, D. S. Su, F. Wei, Toward full exposure of “active sites”: Nanocarbon electrocatalyst with surface enriched nitrogen for superior oxygen reduction and evolution reactivity. *Adv. Funct. Mater.* **24**, 5956–5961 (2014).
44. G.-L. Tian, M.-Q. Zhao, D. Yu, X.-Y. Kong, J.-Q. Huang, Q. Zhang, F. Wei, Nitrogen-doped graphene/carbon nanotube hybrids: In situ formation on bifunctional catalysts and their superior electrocatalytic activity for oxygen evolution/reduction reaction. *Small* **10**, 2251–2259 (2014).
45. Y. Ito, W. Cong, T. Fujita, Z. Tang, M. Chen, High catalytic activity of nitrogen and sulfur co-doped nanoporous graphene in the hydrogen evolution reaction. *Angew. Chem. Int. Ed.* **54**, 2131–2136 (2015).
46. I. Y. Jeon, S. Zhang, L. Zhang, H. J. Choi, J. M. Seo, Z. Xia, L. Dai, J. B. Baek, Edge-selectively sulfurized graphene nanoplatelets as efficient metal-free electrocatalysts for oxygen reduction reaction: The electron spin effect. *Adv. Mater.* **25**, 6138–6145 (2013).
47. J. Long, X. Xie, J. Xu, Q. Gu, L. Chen, X. Wang, Nitrogen-doped graphene nanosheets as metal-free catalysts for aerobic selective oxidation of benzylic alcohols. *ACS Catal.* **2**, 622–631 (2012).
48. A. Taylor, The study of carbon by the Debye-Scherrer method. *J. Sci. Instrum.* **18**, 90 (1941).
49. F. Tuinstra, J. L. Koenig, Raman spectrum of graphite. *J. Chem. Phys.* **53**, 1126–1130 (1970).
50. M. J. Matthews, M. A. Pimenta, G. Dresselhaus, M. S. Dresselhaus, M. Endo, Origin of dispersive effects of the Raman **D** band in carbon materials. *Phys. Rev. B* **59**, R6585–R6588 (1999).
51. A. Shen, Y. Zou, Q. Wang, R. A. W. Dryfe, X. Huang, S. Dou, L. Dai, S. Wang, Oxygen reduction reaction in a droplet on graphite: Direct evidence that the edge is more active than the basal plane. *Angew. Chem. Int. Ed.* **53**, 10804–10808 (2014).
52. W. Yuan, Y. Zhou, Y. Li, C. Li, H. Peng, J. Zhang, Z. Liu, L. Dai, G. Shi, The edge- and basal-plane-specific electrochemistry of a single-layer graphene sheet. *Sci. Rep.* **3**, 2248 (2013).
53. J. Jiang, J. Turnbull, W. Lu, P. Boguslawski, J. Bernholc, Theory of nitrogen doping of carbon nanoribbons: Edge effects. *J. Chem. Phys.* **136**, 014702 (2012).
54. D. Usachov, O. Vilkov, A. Grüneis, D. Haberer, A. Fedorov, V. K. Adamchuk, A. B. Preobrajenski, P. Dudin, A. Barinov, M. Oehzelt, C. Laubschat, D. V. Yvalikh, Nitrogen-doped graphene: Efficient growth, structure, and electronic properties. *Nano Lett.* **11**, 5401–5407 (2011).
55. H. S. Kim, H. S. Kim, S. S. Kim, Y.-H. Kim, Atomistic mechanisms of codoping-induced p- to n-type conversion in nitrogen-doped graphene. *Nanoscale* **6**, 14911–14918 (2014).
56. H. Liu, Y. Liu, D. Zhu, Chemical doping of graphene. *J. Mater. Chem.* **21**, 3335–3345 (2011).
57. C. H. Choi, H.-K. Lim, M. W. Chung, J. C. Park, H. Shin, H. Kim, S. I. Woo, Long-range electron transfer over graphene-based catalyst for high-performing oxygen reduction reactions: Importance of size, N-doping, and metallic impurities. *J. Am. Chem. Soc.* **136**, 9070–9077 (2014).
58. H. Kim, K. Lee, S. I. Woo, Y. Jung, On the mechanism of enhanced oxygen reduction reaction in nitrogen-doped graphene nanoribbons. *Phys. Chem. Chem. Phys.* **13**, 17505–17510 (2011).
59. L. Lai, J. R. Potts, D. Zhan, L. Wang, C. K. Poh, C. Tang, H. Gong, Z. Shen, J. Lin, R. S. Ruoff, Exploration of the active center structure of nitrogen-doped graphene-based catalysts for oxygen reduction reaction. *Energy Environ. Sci.* **5**, 7936–7942 (2012).
60. J. Y. Cheon, J. H. Kim, J. H. Kim, K. C. Goddeti, J. Y. Park, S. H. Joo, Intrinsic relationship between enhanced oxygen reduction reaction activity and nanoscale work function of doped carbons. *J. Am. Chem. Soc.* **136**, 8875–8878 (2014).
61. M. W. Chung, C. H. Choi, S. Y. Lee, S. I. Woo, Dimensionality-dependent oxygen reduction activity on doped graphene: Is graphene a promising substrate for electrocatalysis? *Nano Energy* **11**, 526–532 (2015).
62. R. Eba Medjo, B. Thiodjio Sendja, J. Mane Mane, P. Owono Ateba, A study of carbon nanotube contamination by XANES spectroscopy. *Phys. Scr.* **80**, 045601 (2009).
63. D. Pacilé, J. C. Meyer, A. Fraile Rodríguez, M. Papagno, C. Gómez-Navarro, R. S. Sundaram, M. Burghard, K. Kern, C. Carbone, U. Kaiser, Electronic properties and atomic structure of graphene oxide membranes. *Carbon* **49**, 966–972 (2011).

64. B. J. Schultz, C. J. Patridge, V. Lee, C. Jaye, P. S. Lysaght, C. Smith, J. Barnett, D. A. Fischer, D. Prendergast, S. Banerjee, Imaging local electronic corrugations and doped regions in graphene. *Nat. Commun.* **2**, 372 (2011).
65. Z. Hou, X. Wang, T. Ikeda, K. Terakura, M. Oshima, M.-A. Kakimoto, Electronic structure of N-doped graphene with native point defects. *Phys. Rev. B* **87**, 165401 (2013).
66. L. Mino, G. Agostini, E. Borfecchia, D. Gianolio, A. Piovano, E. Gallo, C. Lamberti, Low-dimensional systems investigated by x-ray absorption spectroscopy: A selection of 2D, 1D and 0D cases. *J. Phys. D Appl. Phys.* **46**, 423001–423072 (2013).
67. Z. Luo, S. Lim, Z. Tian, J. Shang, L. Lai, B. MacDonald, C. Fu, Z. Shen, T. Yu, J. Lin, Pyridinic N doped graphene: Synthesis, electronic structure, and electrocatalytic property. *J. Mater. Chem.* **21**, 8038–8044 (2011).
68. Y. Okamoto, First-principles molecular dynamics simulation of O₂ reduction on nitrogen-doped carbon. *Appl. Surf. Sci.* **256**, 335–341 (2009).
69. H. Dau, C. Limberg, T. Reier, M. Risch, S. Roggan, P. Strasser, The mechanism of water oxidation: From electrolysis via homogeneous to biological catalysis. *ChemCatChem* **2**, 724–761 (2010).
70. I. C. Man, H.-Y. Su, F. Calle-Vallejo, H. A. Hansen, J. I. Martínez, N. G. Inoglu, J. Kitchin, T. F. Jaramillo, J. K. Nørskov, J. Rossmeisl, Universality in oxygen evolution electrocatalysis on oxide surfaces. *ChemCatChem* **3**, 1159–1165 (2011).
71. T. Maiyalagan, K. A. Jarvis, S. Therese, P. J. Ferreira, A. Manthiram, Spinel-type lithium cobalt oxide as a bifunctional electrocatalyst for the oxygen evolution and oxygen reduction reactions. *Nat. Commun.* **5**, 3949 (2014).
72. J. Masa, W. Xia, I. Sinev, A. Zhao, Z. Sun, S. Grutzke, P. Weide, M. Muhler, W. Schuhmann, Mn_xO_y/NC and Co_xO_y/NC nanoparticles embedded in a nitrogen-doped carbon matrix for high-performance bifunctional oxygen electrodes. *Angew. Chem. Int. Ed.* **53**, 8508–8512 (2014).
73. Y. Li, H. Dai, Recent advances in zinc-air batteries. *Chem. Soc. Rev.* **43**, 5257–5275 (2014).

Acknowledgments

Funding: This work was supported by Nanyang Technological University startup grant (M4080977.120); Singapore Ministry of Education Academic Research Fund (AcRF) Tier 1 (M4011021.120); National Research Foundation, Prime Minister's Office, Singapore under its Campus for Research Excellence and Technological Enterprise (CREATE) program; Air Force Office of Scientific Research (FA-9550-12-1-0037); and NSF (CMMI-1400274). **Author contributions:** H.B.Y., L.D., and B.L. conceived and designed the experiments. H.B.Y. carried out synthesis of the catalysts and performed the experiments on electrochemical testing. S.-F.H. and H.M.C. performed the XANES characterization. J.M., J.C., and H.B.T. contributed to the data analysis. X.W. performed the UPS study. L.Z. characterized the samples using XRD. J.G. contributed to the TGA experiments. R.C. helped on the water electrolysis studies. L.D. and B.L. supervised the entire project, and H.B.Y., L.D., and B.L. wrote the manuscript. **Competing interests:** The authors declare that they have no competing interests. **Data and materials availability:** All data needed to evaluate the conclusions in the paper are present in the paper and/or the Supplementary Materials. Additional data related to this paper may be requested from the authors.

Submitted 17 August 2015

Accepted 24 March 2016

Published 22 April 2016

10.1126/sciadv.1501122

Citation: H. B. Yang, J. Miao, S.-F. Hung, J. Chen, H. B. Tao, X. Wang, L. Zhang, R. Chen, J. Gao, H. M. Chen, L. Dai, B. Liu, Identification of catalytic sites for oxygen reduction and oxygen evolution in N-doped graphene materials: Development of highly efficient metal-free bifunctional electrocatalyst. *Sci. Adv.* **2**, e1501122 (2016).

Identification of catalytic sites for oxygen reduction and oxygen evolution in N-doped graphene materials: Development of highly efficient metal-free bifunctional electrocatalyst

Hong Bin Yang, Jianwei Miao, Sung-Fu Hung, Jiazang Chen, Hua Bing Tao, Xizu Wang, Liping Zhang, Rong Chen, Jiajian Gao, Hao Ming Chen, Liming Dai and Bin Liu (April 22, 2016)
Sci Adv 2016, 2:
doi: 10.1126/sciadv.1501122

This article is published under a Creative Commons license. The specific license under which this article is published is noted on the first page.

For articles published under [CC BY](#) licenses, you may freely distribute, adapt, or reuse the article, including for commercial purposes, provided you give proper attribution.

For articles published under [CC BY-NC](#) licenses, you may distribute, adapt, or reuse the article for non-commercial purposes. Commercial use requires prior permission from the American Association for the Advancement of Science (AAAS). You may request permission by clicking [here](#).

The following resources related to this article are available online at <http://advances.sciencemag.org>. (This information is current as of April 27, 2016):

Updated information and services, including high-resolution figures, can be found in the online version of this article at:

<http://advances.sciencemag.org/content/2/4/e1501122.full>

Supporting Online Material can be found at:

<http://advances.sciencemag.org/content/suppl/2016/04/19/2.4.e1501122.DC1>

This article **cites 73 articles**, 6 of which you can be accessed free:

<http://advances.sciencemag.org/content/2/4/e1501122#BIBL>

Science Advances (ISSN 2375-2548) publishes new articles weekly. The journal is published by the American Association for the Advancement of Science (AAAS), 1200 New York Avenue NW, Washington, DC 20005. Copyright is held by the Authors unless stated otherwise. AAAS is the exclusive licensee. The title *Science Advances* is a registered trademark of AAAS